

---

This is an electronic reprint of the original article.  
This reprint may differ from the original in pagination and typographic detail.

Jovanovic, N.; Riwanto, B.; Niemelä, P.; Mughal, M. Rizwan; Praks, J.

## Design of Magnetorquer-Based Attitude Control Subsystem for FORESAIL-1 Satellite

*Published in:*  
IEEE Journal on Miniaturization for Air and Space Systems

*DOI:*  
[10.1109/JMASS.2021.3093695](https://doi.org/10.1109/JMASS.2021.3093695)

Published: 01/12/2021

*Document Version*  
Publisher's PDF, also known as Version of record

*Published under the following license:*  
CC BY

*Please cite the original version:*  
Jovanovic, N., Riwanto, B., Niemelä, P., Mughal, M. R., & Praks, J. (2021). Design of Magnetorquer-Based Attitude Control Subsystem for FORESAIL-1 Satellite. *IEEE Journal on Miniaturization for Air and Space Systems*, 2(4), 220-235. Article 9468712. <https://doi.org/10.1109/JMASS.2021.3093695>

---

This material is protected by copyright and other intellectual property rights, and duplication or sale of all or part of any of the repository collections is not permitted, except that material may be duplicated by you for your research use or educational purposes in electronic or print form. You must obtain permission for any other use. Electronic or print copies may not be offered, whether for sale or otherwise to anyone who is not an authorised user.

# Design of Magnetorquer-Based Attitude Control Subsystem for FORESAIL-1 Satellite

N. Jovanovic<sup>ID</sup>, B. Riwanto<sup>ID</sup>, P. Niemelä<sup>ID</sup>, M. Rizwan Mughal<sup>ID</sup>, and J. Praks<sup>ID</sup>, *Member, IEEE*

**Abstract**—The magnetorquer-based attitude control system capable of attaining high spin rates and precise pointing control is required for a 3U CubeSat satellite FORESAIL-1. The satellite, developed by the Finnish Centre of Excellence, needs to maintain a spin rate of 24°/s and precise pointing of the spin axis toward the Sun for the particle telescope instrument, as well as to reach 130°/s spin rate for the deployment of the plasma brake. Mission requirements analysis and attitude system requirements derivation are presented, followed by actuator tradeoff and selection, with a detailed design of the complete attitude control system, including the air-cored type of magnetorquer actuators and their drivers, made of H-bridge and filtering components. The design is based on several theoretical and practical considerations with emphasis on the high-power efficiency, such as effects of parallel and serial magnetorquer connections, modeling the magnetorquers with equivalent circuit models for finding a suitable driving frequency and extrapolation methods for efficient dipole moment usage. The in-house manufacturing process of magnetorquers, using a custom 3-D-printer setup, is described. Finally, the testing and verification are performed, by measuring the performance of the manufactured hardware, circuit simulations, and attitude control simulations. It is shown that the manufactured attitude control system fulfills all system requirements. Simulations also confirm the capability to satisfy mission requirements.

**Index Terms**—Attitude control, CubeSat, magnetorquer, power control.

## I. INTRODUCTION

**I**N THE modernization of the new-space era, nanosatellites have become a significant industry player and their applications are expected to rise exponentially in the near future

Manuscript received March 7, 2021; revised June 15, 2021; accepted June 27, 2021. Date of publication June 30, 2021; date of current version November 18, 2021. This work was supported by the Finnish Centre of Excellence in Research of Sustainable Space, building and launching three FORESAIL missions is funded through the Academy of Finland under Grant 312351, Grant 312390, Grant 312358, Grant 312357, and Grant 312356. (*Corresponding author: N. Jovanovic.*)

N. Jovanovic, B. Riwanto, P. Niemelä, and J. Praks are with the School of Electrical Engineering, Aalto University, 02150 Espoo, Finland (e-mail: nemanja.jovanovic@aalto.fi).

M. Rizwan Mughal is with the School of Electrical Engineering, Aalto University, 02150 Espoo, Finland, and also with the Department of Electrical Engineering, Institute of Space Technology, Islamabad 44000, Pakistan.

Digital Object Identifier 10.1109/JMASS.2021.3093695

due to their low cost and fast development [1]. The ever-increasing applications of nanosatellites prompt a need for further improvements and are pushing the novel techniques in the development of space technologies to their limits [2], [3]. State-of-the-art satellite instruments, to be utilized to their full potentials, could require more power, larger data transfer rates, and highly precise attitude knowledge. These challenges need to be addressed by nanosatellite platforms to enable the use of novel miniaturized payloads.

FORESAIL-1 satellite needs to support two spin-stabilized attitude modes around the major principal axis of inertia, one with an angular velocity of 24°/s and acceptable error of  $\pm 0.24^\circ/\text{s}$ , as well as one with the capability of reaching a spin rate of 130°/s. Acquiring the necessary angular velocity of this magnitude and operating under such circumstances demands reliability, reactivity, and efficiency. There are several nanosatellite missions that were designed with spin-stabilized attitude modes, which include CINEMA [4], RACE [5], DICE [6], ESTCube-1 [7], and ELFIN [8]. CINEMA and RACE are both 3U CubeSats with spin rates of 24°/s and 30°/s, respectively. They provide similar spin rates as required by the FORESAIL-1 precise spin mode. Thus, it is evident that achieving the angular velocity is not a challenge, but keeping it within the allowable tolerance. DICE mission is comprised of two identical 1.5U CubeSats that required 720°/s of angular velocity for the boom deployment. ESTCube-1 is a 1U CubeSat that demonstrated spin rate of 841°/s. Both missions reached much higher rotational energies than the FORESAIL-1 requires, confirming the viability of the goal. Finally, ELFIN is a 3U CubeSat with a stabilized spin rate of 120°/s. Still, several design decisions and constraints may render the spin-up maneuver a considerably long operation, thus increasing the operational costs and faults possibility.

The task of achieving and managing the satellite's attitude state is performed by the attitude control subsystem (ACS) [9]. The main components of these subsystems are actuators that generate torques, driving hardware for delivering power to the actuators, and a control strategy which provides the desired torque output values. Traditionally, the control strategy is run on an active processing unit in loop with attitude determination methods and sensor readings [10]. The ever-demanding nanosatellite missions are the main drivers for improvements and expansion of current attitude control solutions. The technology advancement in nanosatellite reaction

wheels and thrusters for attitude maneuvers has seen significant improvements [11], [12]. Some nanosatellites equipped with thrusters are MarCO [13] and POPSAT-HIP1 [14], while reaction wheels were flown within Aalto-1 [15].

Magnetorquer and reaction wheel actuators are becoming commonplace within nanosatellite platforms [16]–[19]. All of the previously mentioned CubeSat satellites relied on magnetorquers for torque production. The FORESAIL-1 satellite needed a custom solution for magnetorquer-based attitude control with efficient dipole moment production and the use of available volume and power. Furthermore, several additional constraints were imposed by the satellite system. The design, testing, and applicability of manufactured ACS for the FORESAIL-1 satellite mission is presented in this article. It focuses on the hardware and software necessary for the controlled production of torques, including actuators and their driving electronics. A holistic approach is presented, examining a wide range of properties of magnetorquers, driving circuits, and significant effects emerging in relation to the rest of the system. Among the novelties presented in this article that are in-depth magnetorquer analysis using the equivalent circuit model in interaction with the driving circuit and electromagnetic interference (EMI) effects, the in-house magnetorquer manufacturing using a 3-D printer setup and the use of extrapolation methods for efficient use of control output at high angular velocities. Furthermore, the tradeoff between serial and parallel magnetorquer connections and tuning of power conversion circuits are shown. However, control strategies for achieving the desired attitude states and attitude determination matters are not covered.

The remainder of this article is structured as follows. Section II presents detailed information about the FORESAIL-1 attitude control system, starting with the attitude maneuver-related mission requirements, which are used to derive requirements for the ACS. Section III presents the attitude actuator tradeoff analysis and the theoretical basis for the magnetorquer-based attitude control system and the magnetorquer driver circuit's design. Section IV continues with magnetorquer and driver design description and presents manufacturing and testing results. Section V discusses satisfaction of the requirements derived in the first section. The conclusion is presented afterward in Section VI.

## II. FORESAIL-1 MISSION

The mission objectives for FORESAIL-1 are measurements of energetic particle precipitation and solar energetic neutral atoms, and the demonstration of a deorbiting technology. It is the first satellite mission of a multimission project, which aims to improve knowledge and technical capabilities beneficial for the sustainable use of space [20]. The 3U CubeSat satellite will house two main payloads, particle telescope, and plasma brake. The particle telescope (successor to RADMON [21] instrument onboard Aalto-1 satellite [22]) will be measuring radiation characteristics in the low Earth orbit (LEO). Besides the scientific values for the Earth space environment of these measurements, the gained knowledge can help improve the reliability and longevity of future satellites. The plasma

brake payload will demonstrate an affordable and efficient deorbiting technology, a viable solution for reducing space debris [23]. This experiment will provide valuable insights for improvements of propellantless propulsion systems. Aside from payloads, the satellite platform has been designed to ensure reliability and optimum radiation protection, furthering reliable design abilities.

One of the stringent challenges of this mission is to achieve the attitude requirements of both payloads. The particle telescope payload requires precise attitude control, to obtain high-quality measurements. It requires a sun pointing attitude mode with a stable spin around the pointing axis with the angular velocity of  $24^\circ/\text{s}$ . However, the plasma brake requires to attain a significant angular momentum, as the deployment of the plasma brake's 300-m long tether is only possible if sufficient centrifugal force is available throughout the deployment process. For the deployment of first 10 m, the initial spin rate of  $130^\circ/\text{s}$  should be provided by the ACS [23], [24].

### A. Mission Attitude Requirements

Three attitude modes have been identified, which include detumbling, operation mode for particle telescope, and operation mode for plasma brake. Detumble mode is intended for the commissioning phase and recovery scenarios, as a means of providing a known initial state for the payload's attitude modes. Both the particle telescope and plasma brake payloads require spin-up maneuver and the capability to point the spacecraft spin axis in the inertial frame [20]. Additionally, pointing maneuvers between the operation modes are intended for proper aligning of the satellite's spin axis according to the experimental needs.

The detumbling maneuver should be capable of reducing the angular velocities, experienced at the beginning of either experiment, down to the levels from which payload attitude modes can be properly initiated. For simplicity and with a wide margin,  $1^\circ/\text{s}$  is chosen as the upper spin rate limit after the detumbling. Predicting possible angular velocity ranges after the separation from the launch vehicle is difficult due to a large number of factors, among which are satellite parameters and structural tolerances, deployment mechanism characteristics, and launch vehicle vibration interference [25]. However, the highest rotational energy that the FORESAIL-1 satellite's attitude system is expected to handle is during the plasma brake operation. Thus, the detumbling maneuver requirement of the lowest angular velocity from which detumbling shall be achievable corresponds with the required angular velocity of the plasma brake experiment.

The first 10 m of the plasma brake's tether is to be deployed using centrifugal force acting on the tether's end mass. Force is provided through the rotational motion of the satellite obtained with the attitude control system. Angular velocity needed to accomplish this goal is calculated to be  $130^\circ/\text{s}$  [23], which would exert the maximal allowed force without damaging the tether. The angular momentum for the deployment of the remaining length of the 300-m-long tether can then be generated by actuating plasma brake. Additionally, to achieve favorable alignment of the tether with the environmental

TABLE I  
MISSION PHASES WITH ANGULAR VELOCITIES

#	Description	$\omega_0$ [°/s]	$\omega_f$ [°/s]	$\Delta\omega$ [°/s]
1	detumbling	30	0	30
2	pointing maneuver	0	0	5
3	PB spin-up	0	130	130
4	detumbling	130	0	130
5	pointing maneuver	0	0	5
6	PATE spin-up	0	24	24
7	pointing corrections	24	24	10

plasma flow, the maneuver needs to maintain the rotation axis nearly parallel with the Earth's rotation axis, with an accuracy of 5°.

Finally, the particle telescope instrument needs its rotation axis to be maintained toward the Sun direction with a stable spin of  $24 \pm 0.24^\circ/\text{s}$  around it, necessary for the determination of pitch-angle distribution and separation of trapped and precipitating particles [26]. The pointing accuracy of the rotating axis shall be within 3°.

The estimated changes of satellite's angular velocity throughout the mission phases are presented in Table I with seven maneuvers. The first and second columns give initial  $\omega_0$  and final  $\omega_f$  angular velocities during the maneuver, while the last column shows the total accumulated angular velocity change  $\Delta\omega_0$ , after each maneuver. The overall accumulated angular velocity change during the mission is the sum of changes of each maneuver  $\Delta\omega_T = 334^\circ/\text{s}$ .

The attitude requirements posed by all mission phases can be summarized as follows.

- M1* Total angular velocity change that the attitude control system can perform shall be at least  $334^\circ/\text{s}$ .
- M2* Detumbling maneuver shall be able to reduce angular velocities from at least  $130^\circ/\text{s}$  to below  $1^\circ/\text{s}$ .
- M3* Plasma brake spin-up maneuver shall be able to increase the angular velocity around the selected axis up to  $130^\circ/\text{s}$  with the pointing error below 5°.
- M4* Particle telescope spin-up maneuver shall be able to increase the angular velocity around the selected axis up to  $24^\circ/\text{s}$  and maintain it with error smaller than  $0.24^\circ/\text{s}$ , with the pointing error below 3°.

### B. Requirements for Attitude Subsystem

The given mission attitude requirements are transformed to delineated requirements that directly concern the ACS. The satellite platform imposes additional constraints on the selection and design of ACS. The subsystem is to be integrated within a 3U CubeSat, with principal moments of inertia  $I_{x,y,z} = [0.035 \ 0.034 \ 0.009]^T \text{ kg m}^2$ . The platform shall ensure the availability of 500 mW of power and up to 300 g of mass budget for ACS. Also, the EMI, generated by the attitude subsystem is to be minimized, as to not interfere with the Particle Telescope payload measurements.

The minimum angular momentum change that the attitude control system should be capable to execute can be derived from mission requirement M1 by multiplying angular velocity with the greatest moment of the inertia value, giving the value of 0.204 N m s.

From the initial and target angular velocities of mission requirement M2, the necessary range under which attitude and angular momentum shall be controllable can be determined by taking the extremes given there.

The inertial axis pointing stability and resistance to disturbance torques of a spinning satellite improves with the increase of the spin rate. Thus, it is a sufficient requirement to have pointing precision stated in M4, which will also cover the M3 case.

The particle telescope experiment determines necessary actuation coarseness. Adequately quantized control of produced angular impulses is needed to maintain a narrow range of angular velocity error from requirement M4 around the rotation axis and to correct its pointing toward the Sun, which deviates daily almost 1°. Of the two, the angular velocity error is a stronger restriction because of the allowable axis of the Sun pointing error in M4. Then, for a spin around the axis with a major moment of inertia, the smallest producible angular impulse should be lower than  $293 \ \mu\text{Nms}$ . The greatest producible impulse is not set as a requirement but will be posed as the optimization criterion. Still, for stable control, it should be at least an order greater than the environmental disturbance effects. Higher angular impulses reduce the time needed for attitude maneuvers, improving subsystem efficiency.

Three attitude subsystem requirements and one optimization constraint can be summarized from this analysis.

- R1* The minimal angular momentum change shall be 0.204 N m s.
- R2* The attitude control system shall operate, controlling the attitude and angular momentum, over the range of angular velocities  $1^\circ/\text{s} \leq \omega \leq 130^\circ/\text{s}$ .
- R3* The smallest producible angular impulse step shall be  $293 \ \mu\text{Nms}$ .
- OC* The greatest producible angular impulse will be maximized under constraints of the available power, volume and mass budgets.

### III. ATTITUDE CONTROL SYSTEM

While designing the attitude control system for FORESAIL-1, the detailed tradeoff between the available actuator options was performed.

The large angular momentum exchange required by R1, could be achieved by the use of thrusters but they were not selected since a single rotation axis requires four thrusters with very precise positioning and calibration. Moreover, they usually come up with narrow output thrust levels and the propellant residues might interfere with particle telescope measurements.

Reaction wheels are subject to the gyroscopic resistance forces when loaded with significant momentum bias, which can cause difficulties in satisfying the requirement R2. Additional torque margins for compensating gyroscopic forces are necessary. They are suitable for achieving precise pointing and removing errors. Though they inherit nonlinearities of dc-motors and have coarse torque at low rotor spinning rates. These nonlinearities are often not reported in data sheets and they are difficult to estimate; therefore, they are prone to

conflict with the requirement R3. Due to their limited span of angular momentum exchange, the reaction wheels need to be adequately chosen to satisfy requirement R1. The requirement R1 concerns the total momentum exchange during the mission, while the reaction wheels should be able to support only the largest one directional exchange. Table I suggests that biggest one-way angular velocity change would be at least  $180^\circ/\text{s}$ , which translates to minimum angular momentum of  $0.11 \text{ N m s}$ . However, this is necessary for the rotation axis of the payloads, while for the other two axes only the first two phases can be considered, giving  $0.022 \text{ N m s}$ . Reaction wheels with sufficient angular momentum storage are readily available commercially but they are mostly intended for 6U CubeSats [27], [28]. Options for 3U class are scarcer and sufficient momentum storage could be achieved with a combination of two reaction wheels, such as RWP050 and RWP100 [28], but the volume required is substantial. The reaction wheels were not chosen due to significant operational power consumption and volume limitations. They have tendency to build up momentum due to residual losses, e.g., frictional losses and environmental disturbance torques. Over time, this can bring them into saturation, requiring a different type of actuator to desaturate. Thus, the attitude requirements could not be met with the reaction wheel-only solution.

Magnetorquers also have unlimited angular momentum exchange capability, but the torque is generated due to interaction with the environment, directly satisfying requirement R1 without additional constraints. Requirements R2 and R3 can be easily fulfilled, with a suitable magnetorquer driver design. However, the producible torque can only be perpendicular to the environmental magnetic field and is not able to continuously counteract disturbance torques. The attitude control methods have to rely on periodical controllability and long-term control. The torque rods, air core, and printed magnetorquers are available for CubeSats with strengths ranging from  $0.1$  to  $0.5 \text{ A m}^2$  [18], [29]–[31]. With geomagnetic field being, on average, above  $10 \mu\text{T}$  in a plane normal with the Earth's rotational axis at altitudes lower than  $800 \text{ km}$ , more than  $2 \mu\text{Nm}$  of torque can be expected during the plasma brake spin-up maneuver, which is in a ballpark of ten times stronger than the expected environmental disturbance torques.

From this tradeoff analysis, the magnetorquer-based attitude control system is the only viable option to fulfill attitude control requirements of FORESAIL-1. Still, the amount of rotational energy involved with spin-up maneuvers is a challenging task and sufficient control precision is needed. For these reasons, we opted to build in-house magnetorquers, accompanying the driver and associated control scheme. Magnetorquer driver provides variable power output over multiple channels with changeable current flow direction thereby providing controlled delivery of the energy to the magnetorquers. The magnetorquers convert the provided electrical energy to the magnetic field, which in interaction with the environment produces angular motion.

### A. Magnetorquers Model

When a voltage source is applied to magnetorquer, a magnetic field is generated around it by the electric current flow.

Magnetorquer's and environmental magnetic fields then interact, producing a torque, which can be viewed as sliding of a magnetorquer's orientation toward the state of the minimum magnetic potential energy. If a magnetorquer is located within a uniform magnetic field, a simplified interaction model can be used instead where the magnetorquer's generated field is represented with a dipole moment. Then, torque  $\vec{\tau}$ , dipole moment  $\vec{M}$ , and local magnetic field  $\vec{B}$  are related as [32]

$$\vec{\tau} = \vec{M} \times \vec{B}. \quad (1)$$

The dipole moment for a single convex-shaped wire loop, which encloses an area  $A$  with the normal  $\hat{n}$  and conducts electric current  $I$  in a counterclockwise direction relative to the normal, is given as their product, and multiplied with the relative magnetic permeability  $\mu_r$  of the magnetic core. The total dipole moment  $\vec{M}$  is calculated as a sum of dipole moments of all  $N$  wire loops it is formed from as

$$\vec{M} = \mu_r I \sum_{i=1}^N A_i \hat{n}. \quad (2)$$

If the dipole moment is re-expressed in terms of the applied voltage instead of supplied current, and the effective area vector  $\vec{A}_e = \sum_{i=1}^N A_i \hat{n}$  is introduced, which denotes the sum of the enclosed areas, equation becomes

$$\vec{M} = \mu_r \vec{A}_e \frac{U}{R} \quad (3)$$

where  $R$  is the magnetorquers resistance. The power consumption is then computed by

$$P = \frac{U^2}{R} = \frac{\|\vec{M}\|^2 R}{\|\vec{A}_e\|^2 \mu_r}. \quad (4)$$

It is evident from (4) that the power consumption per magnetic moment produced can be reduced by increasing the area encompassed by the magnetorquer and using ferromagnetic cores with higher relative magnetic permeability. However, due to geometrical limitations, most of the designs cannot both have large encompassing area and a ferromagnetic core. Thus, three types of the magnetorquers are generally recognized: 1) torque rods; 2) air core; and 3) PCB printed. FORESAIL-1 uses air-cored magnetorquers for attitude control. For the magnetorquer shown in Fig. 1 with the dimensions labeled for width ( $w$ ), height ( $h$ ), depth ( $d$ ), thickness ( $t$ ), inner and outer width ( $w_i = w - t$  and  $w_o = w + t$ ), height ( $h_i = h - t$  and  $h_o = h + t$ ), and wire radius  $r$ , the number of turns  $N$  are calculated as

$$N = \kappa t d \quad (5)$$

where  $\kappa$  is wire packing factor, describing a number of turns of wire for a unit of area. Factor  $\kappa$  is dependent on the height of additional layers on the wire, like insulation and bonding enamel, but also on the performance of the coiling process.

For the shape as on Fig. 1 the effective area and resistance can be approximately calculated with the following formulas, respectively:

$$A_e = Nwh \quad (6)$$

$$R = 2N\rho \frac{w+h}{r^2\pi}. \quad (7)$$

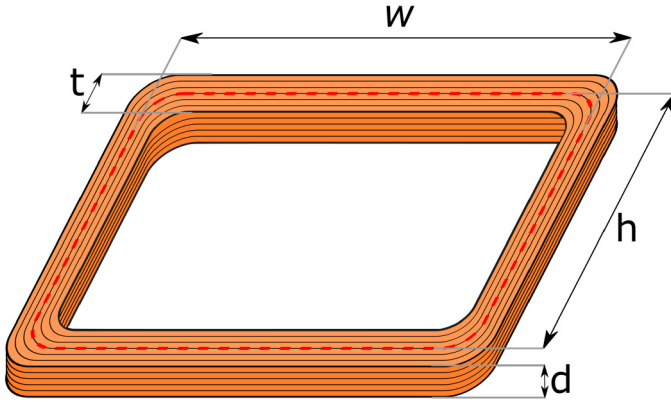


Fig. 1. Air-cored magnetorquer's shape and dimensions.

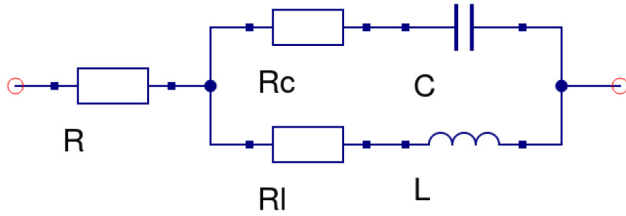


Fig. 2. Equivalent circuit model for magnetorquer.

The voltage to dipole moment dependency equation is

$$U = \vec{M} \frac{2\rho}{\sqrt{\mu_r}\pi} \frac{(w+h)}{whr^2} \quad (8)$$

and for a specific geometry of a coil, this dependency can be adjusted by changing the wire radius.

From the circuit analysis viewpoint, magnetorquers and inductors have little differences and inductor models can be used in magnetorquer's place. However, relative to the inductors, magnetorquers have significantly higher resistance and parasitic capacitance, while inductance is possibly lower. Furthermore, the impedance and resonant frequency are dependent on these properties. In [33], three different inductor circuit models are presented with varying complexities and the ability to reproduce real inductor behavior. The intermediate model, which is shown in Fig. 2, was sufficient for analysis of magnetorquers produced for the FORESAIL-1 satellite.

The dipole moment of the magnetorquer is directly proportional to the driving current, which, in turn, is produced by the driving voltage and depends on the resistance of the magnetorquer and its time constant. The magnetorquer resistance determines the necessary driving voltage for a desired driving current, and due to the wire's temperature coefficient and thermal environment changes in orbit, for some magnetorquer designs, it requires additional consideration. The time constant, given with equation

$$t_c = \frac{L}{R} \quad (9)$$

describes the magnetorquer's change of the dipole moment response with the change of the driving voltage. Attitude control efficiency can deteriorate when the time constant is greater than the necessary control output periods. Also, smaller time

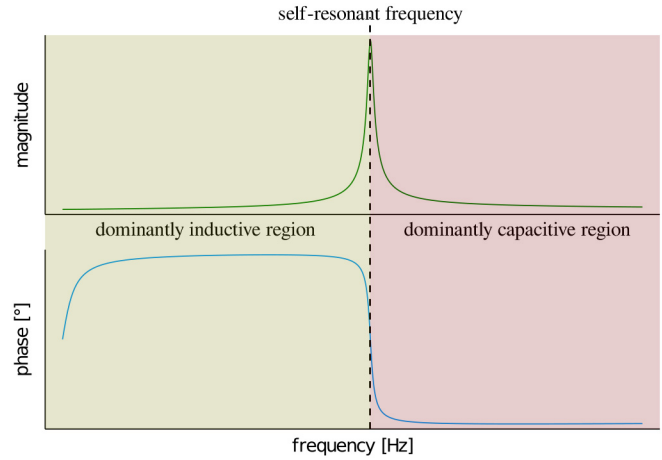


Fig. 3. Typical impedance profile of an inductor.

constants are desirable when frequent magnetorquer switching is done for the purpose of sensor readings.

Depending on the driving circuit, the driving voltage can also have ripple with associated amplitude and frequency. The response of the magnetorquer to the ripple voltage depends on its impedance for that specific frequency. Fig. 3 provides a typical inductor impedance magnitude and phase plot over a range of frequencies, which also applies for the magnetorquers. The peak on the graph is a self-resonant frequency, which divides the frequency range into two regions. The left of the peak is the inductive region and the right side is a capacitive region. At the resonant frequency, the ripple current is lowest in magnitude. Both, ripple voltage and ripple current, are undesirable because of related EMI. While the effects of the ripple voltage can be significantly reduced using conductive shields, the ripple current is more problematic. Magnetorquers generate a relatively strong variable magnetic field, proportional with the ripple current, that spreads over a large volume. Additionally, the power of the ripple components is dissipated without contribution to the dipole moment, leading to a reduction of the power efficiency.

Due to the available physical volume distribution of the FORESAIL-1 satellite, a pair of magnetorquers is designed for each of the three geometrical directions. Magnetorquer coils could be connected in series or in parallel for a single output channel in each axis, or have two channels per axis for each coil. If  $A_{e1}$  and  $R_1$  are the effective area and resistance of one magnetorquer and  $A_{e2}$  and  $R_2$  are those of the other, then the series connection is equivalent to a single magnetorquer with the effective area  $A_{es}$  and resistance  $R_s$  being the sums of the respective values of the two combined magnetorquers, as in equations

$$\begin{aligned} A_{es} &= A_{e1} + A_{e2} \\ R_s &= R_1 + R_2. \end{aligned} \quad (10)$$

In the case of a parallel connection, the effective area and resistance are calculated with equations

$$A_{ep} = \frac{R_1 A_{e2} + R_2 A_{e1}}{R_1 + R_2}$$

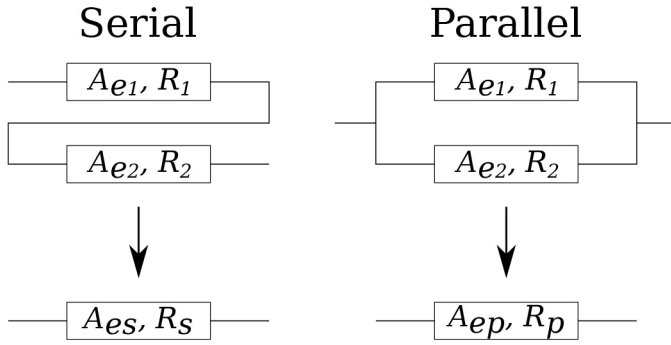


Fig. 4. Serial and parallel connection equivalent magnetorquers.

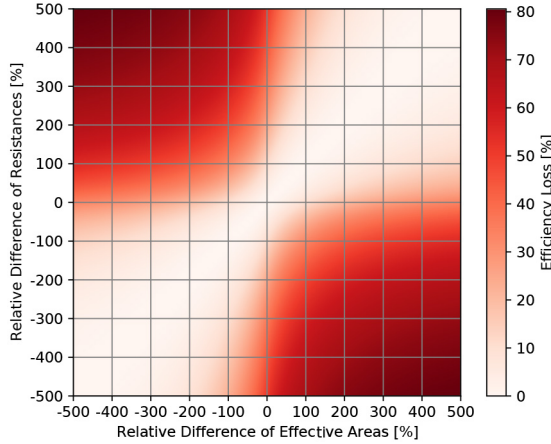


Fig. 5. Efficiency loss for unmatched serial connection.

$$R_p = \frac{R_1 R_2}{R_1 + R_2}. \quad (11)$$

Fig. 4 illustrates equivalent values for both of the connection types.

If the two connected magnetorquers are not matched, their total power consumption will be suboptimal. For serial connection, matching is achieved when area to resistance ratios of the two magnetorquers are equal. Fig. 5 shows the efficiency loss of a serial connection of two magnetorquers. The relative difference of the effective areas is on the  $x$  axis of the plot, and the relative difference of the resistances is on the  $y$  axis. It is notable that the small losses are along the diagonal of the plot box, as the change of area to resistance ratio is also small there.

For the parallel connection, magnetorquers are matched when they have equal effective areas. Fig. 6 shows efficiency losses for the parallel connection of two magnetorquers. The smallest losses are found around the zero relative difference of the effective area.

The tradeoff between the serial and parallel configuration can be guided by the desired total resistance and properties of the used coiling wire. Additionally, the serial configuration can be favored when the effective areas of the paired magnetorquers cannot be matched but their resistances could be properly adjusted. On the other hand, the parallel configuration is more desirable with the pairs of different resistances and the same effective areas, but also to limit effects of temperature-related

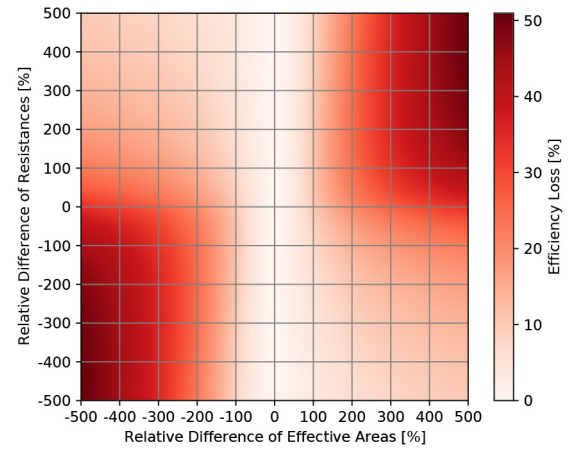


Fig. 6. Efficiency loss for unmatched parallel connection.

resistance change. Third option, with independent driving channels for each magnetorquers, is recommended when the paired magnetorquers are significantly mismatched for either of the cases. Providing dedicated output channels for both magnetorquers would allow applying appropriate voltages to drive them with optimal power. This option adds complexity and additional cost for the driver module, but it can be also seen as the additional level of redundancy for the system.

## B. Magnetorquer Driver

The satellite needs to attain and dissipate significant amount of rotational energy. This can be appropriately done using magnetorquers as they are external momentum exchange actuators without limitations for their operation time as long as the electrical energy is available. However, magnetorquer-based attitude control systems have relatively low angular accelerations, with realistic expectations of about  $2 \times 10^{-4} \text{ }^\circ/\text{s}^2$  for cubesat class of nanosatellites. Additionally, energy management concerns can as well impede the attaining of the attitude goal. Thus, the attitude maneuvers can last for over a week time, as is evident from the ESTCube-1 experience [7]. With small improvements in the torque production and energy use efficiency, the maneuver operation times can be substantially reduced. The satellite will be experiencing high angular velocities, as is demanded by the mission requirements, and to keep the produced dipole moment optimally aligned with the environmental magnetic field, the high output frequency is necessary as well.

On the FORESAIL-1 satellite, the role of the magnetorquer driver is to deliver power to the magnetorquers as dictated by the currently active control strategy executed on the On-Board Computer. Two stages can be distinguished in the driver module, power conversion, and digital control. The digital control stage acts as the receiver of the commands from the On-Board Computer and it generates digital signals for the power conversion stage, which then converts modulated digital signals into analog outputs, delivering the desired voltages and currents to the magnetorquers. The efficiency of this delivery is dependent both on the power intensity and the system's time response. These, in turn, are limited by the magnetorquer's

characteristics, system's power budget and properties of the magnetorquer driver.

Three separately controllable magnetorquer sets, along the  $x$ ,  $y$ , and  $z$  axes of the satellite's body reference frame, are needed to produce any 3-D dipole moment and, thus, at least three mutually independent channels are needed in the power conversion stage. The digital control stage needs to be able to control these channels concurrently.

### C. Digital Control Stage

The digital control stage interprets the received commands, stores the given parameters, and responds with housekeeping data when requested. From the stored values, the output signal value is calculated, depending on the given output mode and the time since the command reception. Later, the output signal is modulated into the PWM signal and a direction selection output, which are directly connected with the power conversion stage.

The output dipole moment can be produced either in the satellite's body or initially fixed reference frame. For the latter, the driver continuously updates the output so that it compensates for the satellites attitude change since the desired output request. The update can be performed with gradient or model-based extrapolation method, which requires setting additional parameters, such as the attitude, angular velocity, and moments of inertia together with the desired dipole moment. Furthermore, timing parameters can be set for magnetic field measuring output turn-off periods and extrapolation output frequency.

Signal outputs are often implemented with zero-order hold. This output strategy sets a constant output value, as commanded, which stays unchanged until the next output command requests the change. This is appropriate for setting the dipole moment in the satellite's body reference frame because there are no other external dependencies. Therefore, spin rates of the FORESAIL-1 maneuver would require a high output update frequency with this output scheme. However, the control law calculations on the controller side and the delivery rate of the commands to the magnetorquer driver board constrain the maximum available update frequency. Fig. 7 shows an example of the frequency effect on the sinusoidal output dipole moment for the zero-order hold on the upper plot and related lost potential dipole moment on the lower plot, for frequency cases of 1, 5, and 10 Hz. Fig. 8 shows required time reduction dependent on the output update frequency for an example maneuver.

The attitude determination and control loop cycle on the On-Board Computer are operated with the frequency of 1 Hz, which is often used and shown to be adequate for target pointing maneuvers control from an inertial frame of reference. It is, as well, sufficient for the spin up maneuver as the stability of the attitude (resistance to external torques) is increased with the higher spin rates, which reduces the required update frequency. However, the output is generated in the satellite's body-fixed reference frame, which needs to be updated according to the satellite's current attitude and angular velocity. This allows for the separation of concerns, where the inertial to

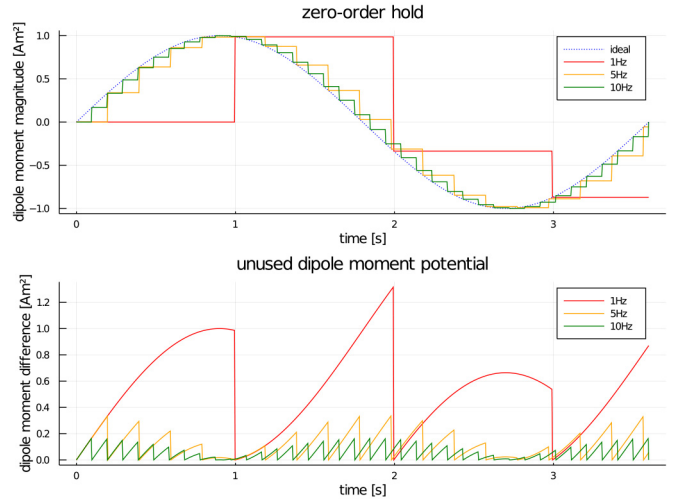


Fig. 7. Example of dipole moment potential loss for three frequencies.

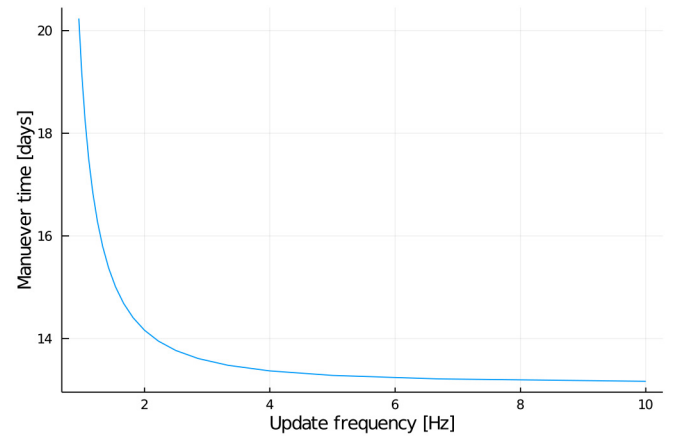


Fig. 8. Example of maneuver time efficiency loss over a range of frequencies.

the body frame translation of the output control vector can be implemented in the magnetorquer driver. Thus, the efficiency loss from low output update frequencies can be avoided with output extrapolation, when dipole moment is given in the inertial reference frame and it is continuously recalculated by the driver in the satellite's body frame as its attitude is changed. While the update frequency of the parameters from the On-Board Computer remains lower. Still, the performance can vary with extrapolation methods.

Gradient extrapolation predicts the dipole moment orientation  $\vec{M}'$  using current angular velocity  $\vec{\omega}$ , given dipole moment  $\vec{M}$  and time  $t$  passed since the dipole moment is set. First, the quaternion of the rotation is calculated as

$$\mathbf{q} = \begin{bmatrix} \vec{e} \sin \frac{\theta}{2} \\ \cos \frac{\theta}{2} \end{bmatrix} \quad (12)$$

where

$$\theta = \|\vec{\omega}\|t \quad (13)$$

and

$$\vec{e} = \frac{\vec{\omega}}{\|\vec{\omega}\|}. \quad (14)$$

Then, the new dipole moment vector is calculated with the following equation, which uses quaternion multiplication and inversion operations, as well as a matrix, which discards surplus value

$$\vec{M}' = \begin{bmatrix} 1 & 0 & 0 & 0 \\ 0 & 1 & 0 & 0 \\ 0 & 0 & 1 & 0 \end{bmatrix} \mathbf{q} \begin{bmatrix} \vec{M} \\ 0 \end{bmatrix} \mathbf{q}^{-1}. \quad (15)$$

Model-based extrapolation uses a mathematical model for rotational dynamics and is superior in keeping the dipole moment well aligned, as long as sufficiently precise parameters are provided. The mathematical model is represented with differential equations

$$\dot{\mathbf{q}} = \frac{1}{2} \begin{bmatrix} 0 & -\omega_z & \omega_y & \omega_x \\ \omega_z & 0 & -\omega_x & \omega_y \\ -\omega_y & \omega_x & 0 & \omega_z \\ -\omega_x & -\omega_y & -\omega_z & 0 \end{bmatrix} \mathbf{q} \quad (16)$$

$$\dot{\vec{\omega}} = (\vec{\omega} \times I\vec{\omega} + \vec{\tau})I^{-1}. \quad (17)$$

The implementation of a numerical integrator is required to use these differential equations. The updated dipole moment is then obtained the same way as in gradient extrapolation, using (15). The requirement for computational power of the microcontroller is therefore high, but the required parameters update frequency is low as the disturbance torques, which are the main driver for losing precision, are relatively low.

Signal pulsing is provided by the digital control stage, letting the output signal to be periodically turned off for short periods of time. Periodical pulsing is needed, simultaneously for all channels, to allow for recurring magnetometer readings, with configurable period  $T_p$  and turn off time  $t_{\text{off}}$ . When pulsing is used, the maximal dipole moment per channel is averaged to

$$M_{\text{max}} = M \left( 1 - \frac{t_{\text{off}}}{T_p} \right). \quad (18)$$

#### D. Power Conversion Stage

Dipole moment is linearly dependent on the current passing through the magnetorquer coils, and so the current would be ideal controllable value. A circuit with a controllable output current usually contains operational amplifiers with a negative feedback loops, which are beneficial for the output stability. The regulation principle of these sources, also called linear, involves the dissipation of excess energy. However, much higher efficiency can be achieved using switched power converters [34]. They use magnetic energy storage of inductors to convert the pulsed voltage source with controllable duty cycle to continuous current flow. Magnetorquer itself can be used for magnetic energy storage, as well, if it has sufficient inductance. For the FORESAIL-1 satellite, a switching power converter with a structure based on the buck converter was selected.

The power conversion stage for a single output channel consists of the full H-bridge and two RLC circuits, forming third-order low pass filters, on magnetorquer output terminals. The design of all three power converters is symmetrical and it is shown in Fig. 9. H-bridge, made of four

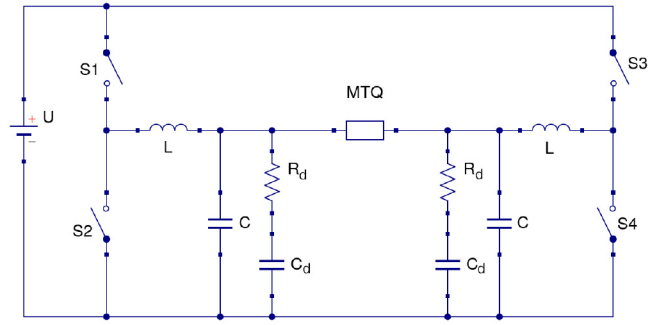


Fig. 9. Magnetorquer driver channel with the LC circuit and H-bridge.

TABLE II  
SWITCHING SCHEMES FOR H-BRIDGE

Mode	PWM	S1	S2	S3	S4
Forward	HIGH	ON	OFF	OFF	ON
	LOW	OFF	OFF	ON	ON
Reverse	HIGH	OFF	ON	ON	OFF
	LOW	OFF	OFF	ON	ON

$N$ -channeled MOSFETs (shown as switches in Fig. 9), is operated by the digital control stage, similarly to synchronous continuous-mode buck converter operation. One of the magnetorquer terminals is grounded by switching on either S2 or S4 MOSFETs for reverse or forward current direction, respectively. The other terminal is driven by an alternating conduction state for MOSFETs S1 and S2 for forward, or S3 and S4 for the reverse current direction. This alternation is done with a PWM signal, whose duty cycle determines the output power level. When either S1 or S3 is conducting, the supply voltage is provided to the RLC circuit and the current is pushed through the inductor, charging the magnetic energy. When S2 or S4 conducts, it makes a closed-circuit loop through which the inductor can persist the current flow, releasing the stored magnetic energy. This switching scheme with the continuous current flow is responsible for high efficiency of voltage conversion. However, it is also possible to leave the lower MOSFET of the driving side switched off if they incorporate the body diode. Table II gives the switching schemes. The efficiency of the power converter is severely reduced when the energy required is low and the current flow cannot be kept continuous. To preserve higher efficiency, the duty cycle of PWM is limited with a lower bound and PWM signal pulsing by the digital control stage is used when the lower dipole moments are needed. Resistors and capacitors labeled  $R_d$  and  $C_d$  are used for damping of the undesired oscillations at the coils self-resonance frequency.

The current flowing out from the H-bridge can be decomposed into the dc and ripple components

$$I_o = I_{\text{DC}} + \delta I. \quad (19)$$

The dc current is a fraction of the maximal magnetorquer current, where the fraction is determined with the PWM duty cycle  $D$  (0%–100%), while the maximal current is dependent on the supply voltage  $U_s$  and magnetorquers resistance

$$I_{\text{DC}} = \frac{D}{100} \frac{U_s}{R}. \quad (20)$$

The ripple current is greatest at the duty cycle of 50%, in which case it is calculated as

$$\delta I = \frac{U_L}{2fL} \quad (21)$$

where  $f$  is the PWM frequency and  $U_L$  and  $L$  are voltage and inductance, respectively, of the inductive element. It is desirable for the ripple current to be low, as it directly affects the dipole moment quality and produced EMI. From (21), a desired minimal inductance  $L_{\min}$  for a given PWM frequency can be calculated after the maximal ripple current has been decided.

The voltage over inductor is

$$U_L = U_s - U_{DC} \quad (22)$$

where  $U_{DC}$  is the dc voltage of the magnetorquer's terminal and is a function of the PWM's duty cycle

$$U_{DC} = \frac{D}{100} U_s. \quad (23)$$

Ripple voltage on the magnetorquer's terminal can be calculated with

$$\delta U = \frac{\delta I}{8Cf}. \quad (24)$$

Thus, a total output voltage  $U_o$  is

$$U_o = U_{DC} + \delta U. \quad (25)$$

While the driving side of the RLC circuit is filtering the switched source signal into a desired dc voltage, the grounded side RLC circuit behaves almost like a short circuit. This allows the magnetorquer to consume most of the provided power. However, both sides tend to cause voltage oscillations on the magnetorquer terminals at their resonant frequency. This oscillation reduces the power efficiency and limits the available voltage level for the magnetorquer. For that reason, the damping resistor and capacitor are necessary. Damping capacitors act as high-pass filters, separating the damping resistor from the dc signal, letting only the oscillating signal to dissipate. The capacitor's value should be sufficiently high to have low impedance at the resonant frequency, while the resistor's value needs to be appropriate to achieve critical damping. There is no direct formula for finding values of damping elements, as the RLC circuit is of the third order. However, using circuit simulation and analysis software for finding satisfying values is a straightforward method.

The magnetorquer also behaves as a band-stop filter in this configuration, and matching of the output ripple voltage frequency and magnetorquer's resonant frequency can be of help, for it will minimize the ripple current through it and related EMI.

The efficiency of the power converter depends on several parameters. The H-bridge MOSFETs dissipate power with their channel resistance and switched on MOSFETs has a small, but still noticeable, on-resistance. Additionally, during the switch time, MOSFETs dissipate power on their channel resistance changing from one extreme to other. This dissipation is increased with higher PWM frequencies as the switching periods are then more numerous. Also, the components of

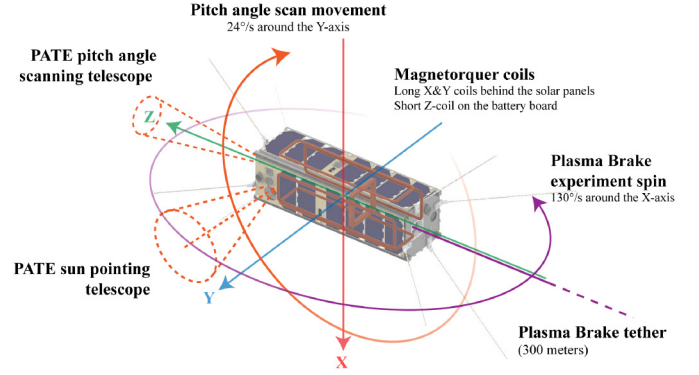


Fig. 10. FORESAIL-1 body frame axes, instruments, and magnetorquers placement.

the LC circuit have nonideal characteristics. Most notably, both capacitors and inductors have ESR values, and while capacitors have a leakage resistance as well, inductors can have parasitic capacitance. Reducing the efficiency losses due to these nonidealities requires a careful selection of components. Finally, efficiency losses can be caused by the eddy currents, which are induced by changing magnetic fields in nearby conductors. Eliminating the presence of the surrounding conductors is rarely an option for some designs. Therefore, minimizing the ripple current through the magnetorquers is important for limiting the losses through the eddy currents as well.

#### IV. DESIGN AND RESULTS

This section describes the design and key results of the magnetorquers, power conditioning stage, and digital control stage. Fig. 10 shows the placement of the magnetorquers within the satellites body and defines the satellite body axes. Furthermore, payload placements and their related spin axes can be seen.

##### A. Magnetorquers

Magnetorquers are manufactured in-house using a 3-D printer with addition of a coiling template, the coil wire tensioning and dispensing mechanisms, together with a specifically generated G-code for the 3-D printer. The coiling setup is presented in Fig. 11, while Fig. 12 shows the coiling template and the friction-based tensioning mechanism. Enameled self bonding wire is used for coiling the magnetorquers and after the 3-D printer completes the winding process, the winding with the template is placed in the reflow oven, where it is cured until the bonding is achieved. After this, the magnetorquer is removed from the template. A template consists of three stacked rectangular cuboid aluminium layers, where the middle one has dimensions corresponding with the magnetorquers inner width, inner height and depth. The dimensions of outer cuboids are larger than the middle in the width and height directions and are extended sufficiently to form a canal that completely covers the magnetorquer. The template layers need to be disassembled for later extraction of the bonded coil.

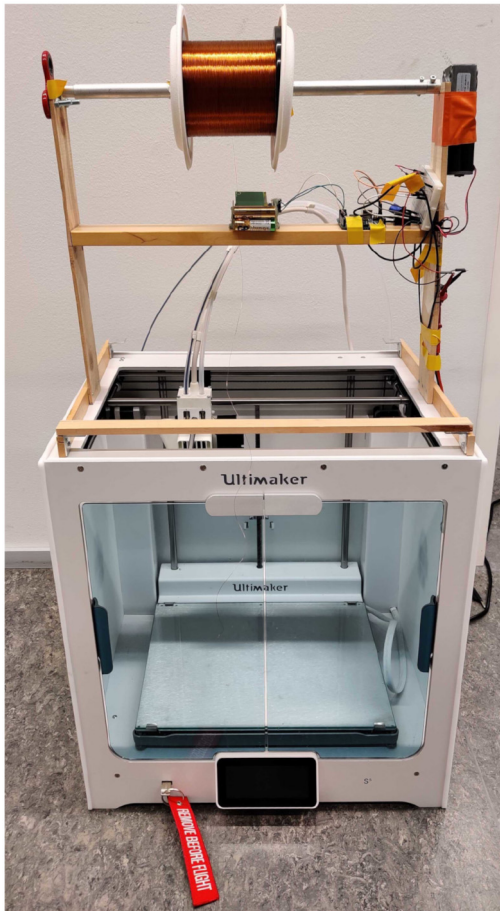


Fig. 11. Setup for coiling of magnetorquers with 3-D printer and the wire dispensing mechanism.

Several challenges had to be addressed to reach a satisfying quality of produced magnetorquers. Keeping a constant tension between the tensioning mechanism and the template required finding a suitable path for the 3-D printer's head, such that there is small variance in the length of the tensioned wire segment. An algorithm finding the optimal path was used for generating the G-code. Furthermore, the wire had to be kept untensioned from the wire spool to the entrance of the tensioning mechanism. This was achieved by attaching a dc motor to the wire spool axle and threading the wire through the tension sensor. A simple controller would unwind the wire spool whenever the tension was sensed by the sensor. The template used for the coil winding can affect the heating and bonding process if it has a significant thermal capacity. The ratio of template mass to coil mass was significantly higher in the case of the short coil and the bonding time had to be extended.

On the FORESAIL-1 satellite, the dedicated volume for the  $x$  and  $y$  axes magnetorquers is located on the back sides of the solar panels. There are four solar panels, comprising the four long faces of the satellite. Therefore, at least two paired physical coils per axis are necessary if the whole volume is to be utilized. For the  $z$  axis magnetorquer, there is volume available on the battery PCB module, which also has the magnetorquer driver electronics integrated. In both cases, there are components placed within the available volumes, so that the

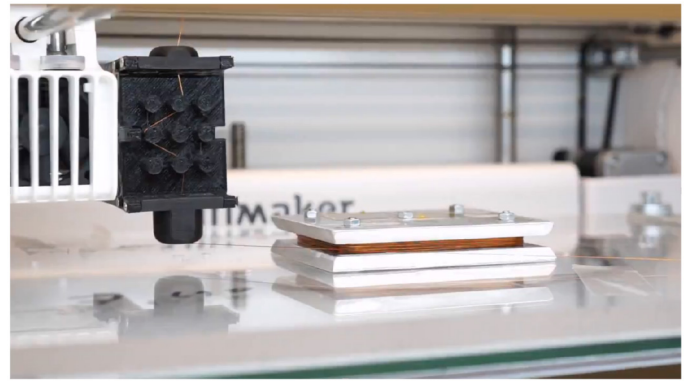


Fig. 12. Tensioning mechanism and the coiling template.

TABLE III  
MAGNETORQUERS PHYSICAL PARAMETERS

Available volume	long	short
width [mm]	270	72
height [mm]	68	68
depth [mm]	2	4
thickness [mm]	8	8
Inner dimension constraints	long	short
width [mm]	260	58
height [mm]	58	55
depth [mm]	2	4
turns	156	513
Measured outer dimensions	long	short
width [mm]	268	71.1
height [mm]	67	68.5
thickness [mm]	4.25	6.65
mass [g]	17.71	29.55
wire packing factor [wires/cm <sup>2</sup> ]	1529.41	1928.57

magnetorquer shapes are limited with a maximum thickness. The available volume section of Table III gives the constraints on the shape of magnetorquers. For simplicity, the  $x$  and  $y$  axes magnetorquers will be referred to as the long and  $z$  axis magnetorquers as the short coils.

Parallel configuration of the paired magnetorquers is preferred for the simpler routing of the connections from the magnetorquer driver board and increased reliability. This choice is further supported with the available volumes allowing for the same designs of the paired magnetorquers and equal effective areas. Additionally, with the pairs of the long coils positioned on the opposite solar panels, a temperature difference between them can be expected to some extent. The power efficiency of parallel configuration is unaffected by the resistance differences caused this way.

For the selected design, if the allowable volume for magnetorquers would be totally filled with copper, the mass would be equal to 265 g. This is less than the constraint placed upon the ACS. However, the magnetorquers can only have lower mass as the packing of copper wires will have gaps and, thus, the constraint cannot be violated. The power efficiency of the magnetorquers is directly proportional to the volume used, while the producible dipole moment strength is proportional to the encompassed effective area. Therefore, using as much of the volume is consistent with following the optimization constraint.



Fig. 13. In-house manufactured magnetorquers.

From the allowable power of 500 mW, 450 mW is reserved for the powering of the magnetorquers. Using this power and satellite platform's bus voltage, the allowable magnetorquer current  $I_{MTQ}$  limit can be calculated. This sets the minimal resistance of magnetorquers,  $R_{MTQ}$ . The coil wire radius should be selected so that the magnetorquers resistance is close to this limit at the minimal expected temperature, in order to maximize the producible dipole moment. A value of the electrical resistivity of copper at the temperature of 0°C should be used. Using (5) and (7), a coil wire with an adequate cross section radius can be selected, while applying dimension margins and the expectation of achieving worse packing factor than reported by the wire manufacturers. Enamelled copper wire with the cross section of 0.028 mm<sup>2</sup>, a diameter of 0.19 mm, and a nominal wire packing factor 2064 wires/cm<sup>2</sup> is found most suitable for the short coils. The same coil wire is selected for the long coils as they outperform short coils due to significantly greater area.

With these parameters, magnetorquer templates could be made for the manufacturing. Considering the margins, the template dimensions and the number of wire turns are derived as provided in the inner dimension constraints section of Table III. The values were given as inputs to the script which generates G-code. Fig. 13 shows the manufactured magnetorquers.

After manufacturing, the outer height, outer width, thickness, and mass of magnetorquers could be measured. Also, the achieved wire packing factor could be calculated. These values are given in the measured outer dimensions section of Table III.

The values of the parallel connection of magnetorquers for the model in Fig. 2 were obtained by measuring the impedance magnitude and phase over the range of frequencies, from 20 Hz to 300 kHz in steps of 1 kHz, using the B&K Precision model 891 LCR meter. The measured and fitted plots in relation to measured and fitted frequency characteristics are shown in Figs. 14 and 15. Plots show that the close fitting of model values is achieved and that the resonant frequencies are at 198.74 kHz and 113.73 kHz for long and short coils, respectively. The model values are given in Table IV, together with

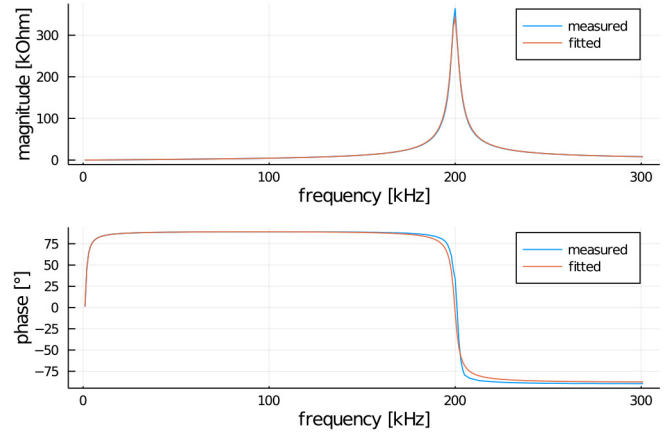


Fig. 14. Impedance magnitude and phase plots for long coil.

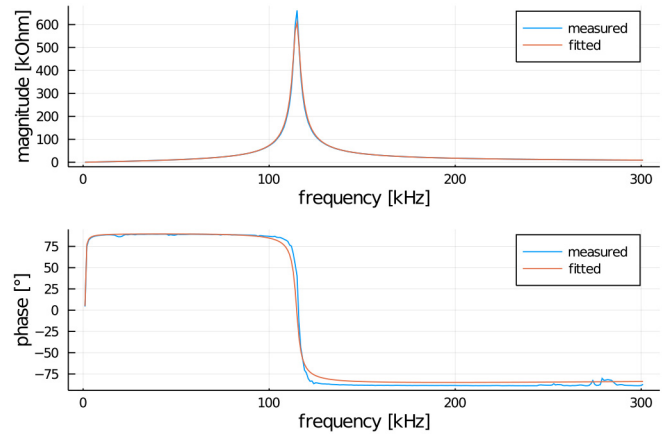


Fig. 15. Impedance magnitude and phase plots for short coil.

TABLE IV  
MAGNETORQUERS' MODEL VALUES

coils	long	short
$R$ [ $\Omega$ ]	0.0	41.61
$R_c$ [ $\Omega$ ]	106.51	689.56
$C$ [pF]	115.34	68
$R_l$ [ $\Omega$ ]	33.92	0.0
$L$ [mH]	5.56	28.8
$f_0$ [kHz]	198.74	113.73
$t_c$ [ $\mu$ s]	164.01	692.14
Effective area [m <sup>2</sup> ]	2.145	2.045
Resistance @0 °C [ $\Omega$ ]	28.45	36.2
Resistance @20 °C [ $\Omega$ ]	30.7	39.08
Resistance @80 °C [ $\Omega$ ]	37.5	47.72
Power @20 °C, 0.15 A m <sup>2</sup> [mW]	149.64	208.75
Power @20 °C, 3.6 V [mW]	423.26	334.08
Dipole moment @20 °C, 3.6 V [A m <sup>2</sup> ]	0.304	0.188

the rest of the calculated magnetorquer parameters, where the relative magnetic permeability is assumed to be as in vacuum,  $\mu_r = 1$ .

### B. Power Converter Stage

For the H-bridge, a COTS driver DRV8838 from Texas Instruments was selected [35]. It provides a fully integrated solution with forward, reverse, brake, and coast output driving functions. The values for discrete components, including inductors and capacitors, have to be selected so that both

TABLE V  
POWER CONVERTER VALUES AT 50% DUTY CYCLE

Coil channel	long	short
$U_{MTQ}$ [V]	1.759	1.746
$I_{MTQ}$ [mA]	51.86	41.96
$\delta I_L$ [mA]	19.99	33.07
$\delta U_{MTQ}$ [mV]	12.49	34.45
$\delta I_{MTQ}$ [ $\mu$ A]	0.043	0.188

driving and grounded RLC circuit sides of the power conversion stage meet desirable performance, under the constraints of operating PWM frequency, available PCB footprint, and parts availability. The biggest concern is to ensure that the ripple currents are below the allowable limits. High ripple currents through the magnetorquer are undesirable as they degrade the quality of output dipole moment and are the greatest contributor to the magnetic field interference. The most sensitive subsystem on the FORESAIL-1 is particle telescope payload, and the estimated permitted field strength is 500 mA/m. The upper limit of the magnetic field generated within the satellite from long coils pairs can be approximated with a Helmholtz coil model [36]. Magnetorquers are not symmetrical like Helmholtz coils, and the generated field is expected to be weaker than the approximation. Taking these approximations into consideration, a limit of 89.6  $\mu$ A is imposed in varying current component. Similarly, for the short coils, the upper limit of the varying current component, 362.48  $\mu$ A, is approximated by the use of the Biot–Savart law [36].

The PWM frequency of a channel should be selected so that it is near the resonant frequency of the magnetorquer, which greatly reduces the ripple current. Therefore, the design choice is to drive long coils with 200 kHz, where the impedance is 293 k $\Omega$ , and short coils with a frequency of 120 kHz and impedance of 183 k $\Omega$ .

The RLC circuit components for channels are further decided, taking into account the selected frequency. The allowed ripple voltage on the magnetorquer terminals is calculated from the allowed ripple current and the impedance. As the limits for the long coils channels are much more stringent, selection of the RLC circuit element values for the long coil channels will also be sufficient for the short coil channel. Using (21) and (24) and applying them for the case of 50% duty cycle, the minimal value of the product of the inductor and capacitor values is found. A combination of  $L = 220$   $\mu$ H and  $C = 1$   $\mu$ F is suitable and with sufficiently high product. The resonant frequency of RLC circuit with these values is 10.73 kHz, which is significantly below the chosen PWM frequencies. The selection of the damping resistor and capacitor was helped with a QUCS circuit simulator, where the RLC circuit model was assembled and the parameter optimization feature was used to find satisfying values. Selected values are 10  $\mu$ F for capacitor and 5  $\Omega$  for resistor. The calculated voltage and current values of the power converter channels are given in Table V. The table also contains values of ripple voltages and ripple currents obtained from the simulation. These values are within the allowed limits.

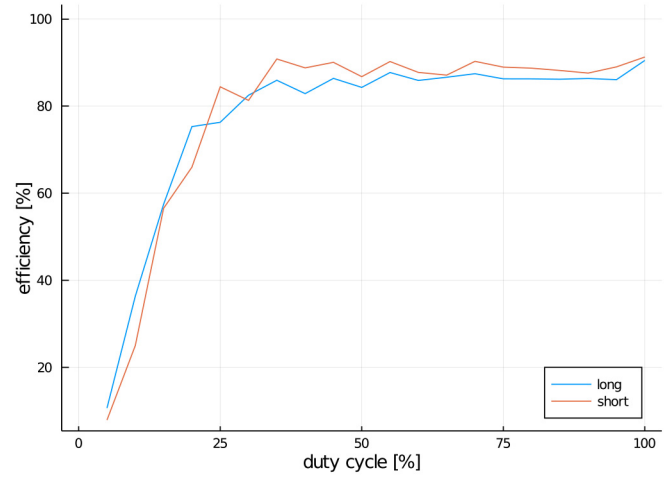


Fig. 16. Power efficiency.

Finally, the power input and output measurements have been taken from the manufactured magnetorquer driver supplied with the power analyzer and connected with electric load. The electric load was configured to the resistance of the magnetorquers and the measurements were taken while varying the PWM duty cycle. The efficiency plots of power conversions for long and short coils are given in the Fig. 16, showing efficiencies of around 90% with duty cycles above 30%. The idle power consumption of the magnetorquer driver board was measured to be 21.6 mW.

### C. Digital Control Stage

The microcontroller selected for the digital control stage is Texas Instruments' MSP430FR5739 [37]. However, the lack of floating-point unit calls for a cautious approach in the implementation of the control output extrapolation modes, in order to achieve the desired output frequency and not exceed limited memory available.

It is equipped with five timer modules, of which one is dedicated for time keeping and management in milliseconds and three for driving the PWM signals for each of power converter channels. One UART module is connected to the external RS485 transceiver and is used for communication with the On-Board Computer. Also, two analog-to-digital inputs are monitoring supply voltage and current consumption for magnetorquer drivers' health status reporting.

Timers for the PWM signals are supplied with a 24-MHz clock and configured to count on every tick upward until the selected period stored in a 16-BIT register, after which the counting is restarted from 0. A compare register is loaded with the value of duty cycle off time. The range of available frequencies is from 3.662 Hz to 12 MHz. However, high frequencies will have poor duty cycle resolution. PWM frequencies at 240 kHz and lower are preferable as duty cycle can be set with the accuracy of nearly 1% and better. The PWM duty-cycle step, expressed in percentage, can be calculated as

$$\Delta DC = \frac{f_{PWM}}{240 \text{ kHz}} \quad (26)$$

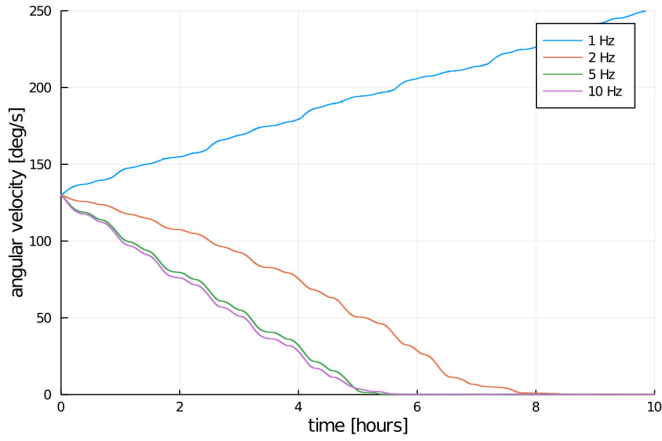


Fig. 17. Detumble maneuver simulations.

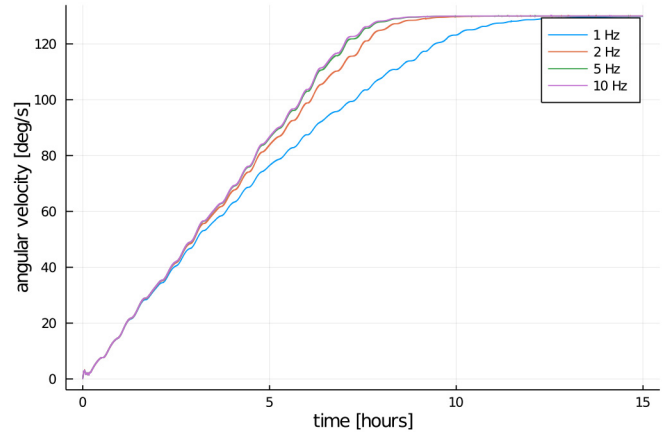


Fig. 19. Plasma brake spin-up maneuver simulations.

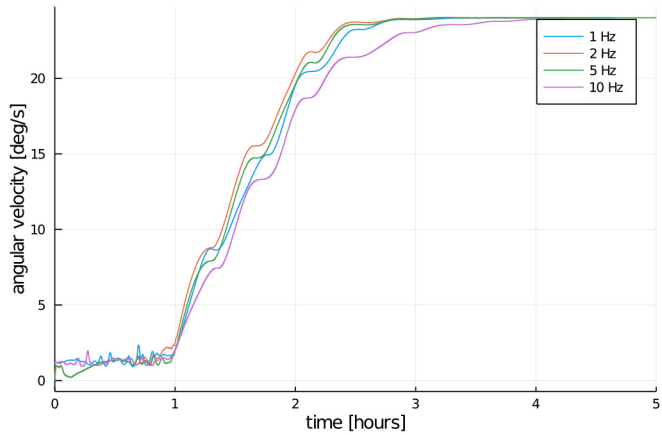


Fig. 18. Particle telescope spin-up maneuver simulations.

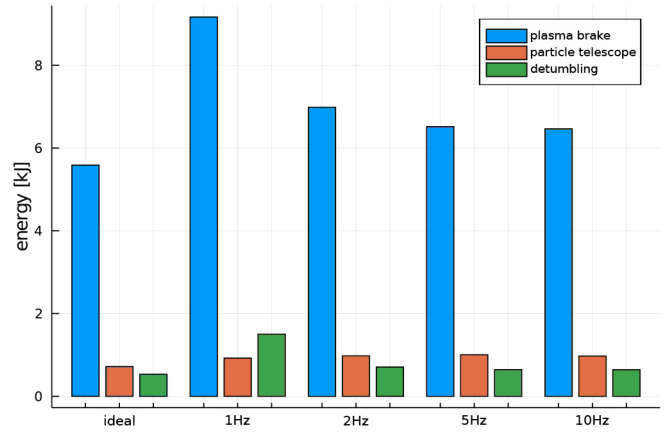


Fig. 20. Energy consumed during the attitude maneuvers.

giving the values for channels of  $\Delta DC_{\text{long}} = 0.83\%$  and  $\Delta DC_{\text{short}} = 0.5\%$ .

Attitude control and dynamics simulations were conducted to analyze the performance of the attitude control maneuvers with output update frequency varied in values of 1, 2, 5, and 10 Hz. The simulation included the effects of the gravity gradient, solar pressure, and aerodynamic drag disturbance torques. Additionally, the produced dipole moment was proportionally reduced to compensate for the magnetometer reading time when the dipole moment actuation has to be temporarily halted. This is presented in Figs. 17–19 for detumbling and spin-up maneuvers for particle telescope and plasma brake, respectively. The detumbling plot shows that the frequency of 1 Hz was not sufficient to guarantee the success of the maneuver, unlike for the higher frequencies. The spin-up maneuver simulations have reached the desired attitude targets for all cases. The detumbling and the plasma brake maneuvers also show the tendency of shorter maneuver times with higher output frequencies. However, this is not the case with particle telescope manoeuvre simulations. This is due to smaller initial angular velocity errors resulting in smaller dipole moments generated, and greater significance of environmental effects for a shorter duration needed for this maneuver. Additionally, the power consumption is compared. While the simulated

particle telescope and plasma brake spin-up maneuvers from Figs. 18 and 19 were used in this comparison, the detumbling maneuver was repeated with starting angular velocity of  $80^\circ/\text{s}$  to avoid the unstable case. Fig. 20 shows the tendency of lesser energy needs with higher frequencies for detumbling and plasma brake cases, while the particle telescope maneuver is with low variation over different output frequencies.

## V. DISCUSSION

The theoretical considerations of magnetorquers include the equivalent circuit model and equations for equivalent serial and parallel configurations of magnetorquers. Equivalent circuit model exposes and helps inspect the magnetorquers' response to the drivers output switching side effects such as ripple voltage. Magnetorquers' self-resonant frequency can be a significant parameter for the calibration of the driver performance and the output signal cleanliness. Understanding the differences between serial and parallel magnetorquer configurations is important for achieving good efficiency. For the FORESAIL-1 mission, the selection of the parallel configuration alleviates part of the efficiency losses related with the temperature changes.

The digital control stage was focused on achieving high output frequencies, for better performance and lower energy consumption. The use of extrapolation methods reduced the

necessary communication rate between the on-board computer and the driver. The effects of varying output frequency were demonstrated. Extrapolation methods to achieve desired output frequencies are explained and implemented in the digital control stage of the driver.

The power conversion stage introduced a driver topology in the form of two buck converters. One important design driver was reduction of the related electro-magnetic interference. Though a simplistic EMI analysis was used, it still provides a valuable general design guide.

The design and results were presented for the three constituent parts of the magnetorquer-based ACS for the FORESAIL-1 satellite. It remains to evaluate how the whole system satisfies the attitude system requirements derived in the introduction and to demonstrate the simulated performance of mission maneuvers.

The choice of the magnetorquers as the actuators was sufficient to directly satisfy the first ACS requirement R1. In interaction with the environmental geomagnetic field, the torque produced is only limited to the available electrical energy. A necessary precondition is that the generated torque is strong enough to dominate over the environmental disturbance torques. This is, however, not considered an issue as the disturbances are relatively weak. Also, the control subsystem design was driven with the optimization criterion OC, which resulted in the available dipole moment outputs for long and short coils equal to 0.304 and 0.188 A m<sup>2</sup>, respectively. Over the duration of one orbit, the producible angular impulse is significantly greater than the angular impulse from the disturbances.

The requirement R2, needed the attitude system to remain operational and able to produce usable output torque throughout the conditions of maneuvers. Although torque produced by magnetorquers depends on the surrounding magnetic field and limits the output generation only to a plane at any given moment, the control provides 3-D output coverage over the mission orbit. Also, the output torque should be producible under the angular velocities of up to 130 °/s. This requirement can be satisfied with sufficiently high output update frequency and low output response times. As demonstrated with the detumbling simulations, there is a limit on the lowest output update frequency. The simulation of the plasma brake spin-up maneuvers with different output update frequencies, as shown in Fig. 19, confirms that even the frequency of 1 Hz is sufficient. The higher frequencies are beneficial for decreasing the maneuver time, though for the frequencies above 5 Hz, the improvements are minor. The magnetorquer driver supports the output frequencies in the range of 1–50 Hz. The response of the output torque depends on the latency of the digital control stage processing loop and the time constant of a combined power conversion stage and a magnetorquer. For the same reason that the damping resistor of the power conversion stage was found using the simulation, the circuit having a third-order differential equation model, the analytical method to find the time constant was not attempted. However, with the chosen power conversion stage elements and magnetorquer equivalent circuit model values, it can be expected that the time constant contribution of magnetorquers is dominating. Table IV gives the time constant values of the magnetorquers to be below

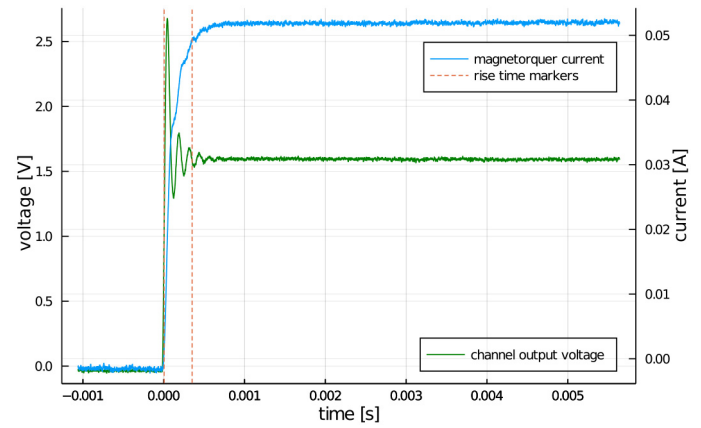


Fig. 21. Long-coil magnetorquer current rise time.

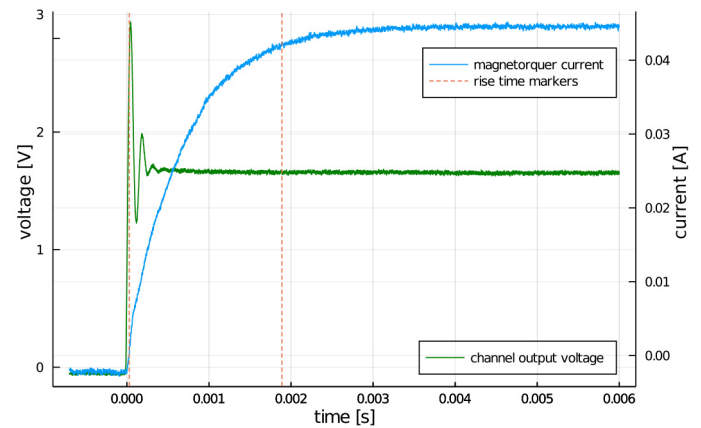


Fig. 22. Short-coil magnetorquer current rise time.

1 ms for both designs, from which the rise time of the output dipole moment is expected to be below 2 ms. These expectations are confirmed by the oscilloscope measurements of the magnetorquer current, provided in Fig. 21 for long and Fig. 22 for short coils and measured rise times of 1.861 and 0.347 ms, respectively. When driving the output with the frequency of 10 Hz, it will be at the desired value for at least 98 % of the time. All these factors amount to a sufficiently good output torque production and satisfaction of the requirement R2.

The requirement R3 prescribes a proper quantization of the producible angular impulses. The magnetorquer driver achieves this by controlling both dipole moment intensity and its duration. While the magnetorquer driver can change the output dipole moment with the frequency of up to 50 Hz, the producible angular momentum is limited by the onboard computer's control loop frequency, which is 1 Hz. Using the equation for the dipole moment (3) and duty-cycle steps, the smallest producible dipole moments for the long and short coils are 2.253 and 1.017 mA m<sup>2</sup>. At the highest expected environmental geomagnetic field strength of around 50  $\mu$ T, the smallest producible angular impulses are 112.641  $\mu$ Nms for long and 50.843  $\mu$ Nms for short coil. With both values being under the maximum value of 293  $\mu$ Nms, the requirement R3 is satisfied.

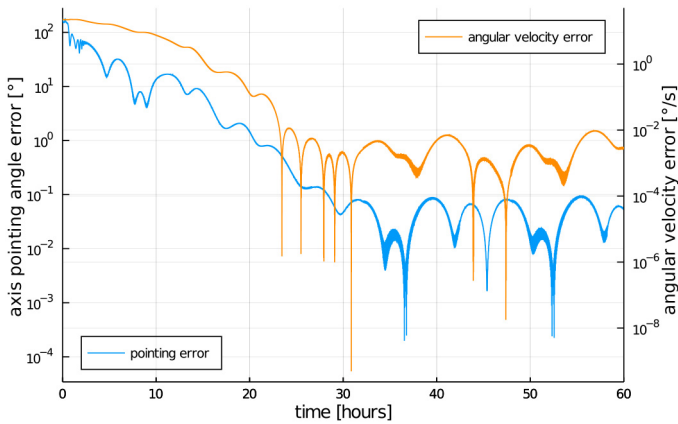


Fig. 23. Particle telescope pointing axis angle and angular velocity errors.

The producible angular moment was also a subject of the optimization constraint OC, with the aim to maximize its value under the constraints of permissible mass, volume, and power consumption. With the available magnetorquer volume, the mass constraint could not be violated. Thus, the mass is not a factor for the optimization and the whole available volume could have been utilized for getting the highest output dipole moment and with it the highest angular impulse, as well as the lowest power consumption per unit of dipole moment. The coiling wire cross section was selected so that the magnetorquers would reach near the limiting power consumption at the maximum supplied voltage, with the significant filling of the available volume. However, due to the limitations of the magnetorquer coiling process and difficulties to predict resulting wire packing factors, significant margins were needed. The achieved packing factor for long coils at  $1529.41 \text{ wires/cm}^2$  is significantly below  $2064 \text{ wires/cm}^2$  as stated by the wire manufacturer. Short coils achieved much closer packing factors of  $1928.57 \text{ wires/cm}^2$ . Still, both designs managed to remain within the given constraints and provide satisfying maximum dipole moment outputs.

Subsystem requirement R1, which was discussed at the beginning of this section, also implies the fulfillment of the mission requirement M1. Requirement R1 is restatement of M1 in terms relevant for the attitude subsystem design.

Successful detumbling maneuver has already been shown with the plot in Fig. 17 with output frequencies of 2 Hz and higher, as well as successful spin-up maneuvers for the particle telescope and the plasma brake with plots in Figs. 18 and 19. However, Fig. 23 additionally shows the pointing angle and the angular velocity error state values, confirming that beside reaching the necessary state, the ACS is capable of remaining stable, therefore satisfying all remaining mission requirements M2, M3 and M4.

## VI. CONCLUSION

A detailed analysis, design, and evaluation of ACS for the FORESAIL-1 CubeSat has been presented. The analysis started from the mission requirements and satellite platform constraints, from which the subsystem requirements were

derived. Among several attitude actuators, it was demonstrated that custom-made magnetorquers are the most appropriate. A theoretical model of magnetorquers, driver power output and control electronics was presented. Following the subsystem requirements and the optimization constraint, design parameters were found, and the subsystem was manufactured. Evaluation and testing were conducted on the subsystem parts. Magnetorquers characteristics were measured, the performance of power converter channels was tested, and the functionality of digital control stage has been evaluated. It was shown that all related subsystem requirements have been satisfied. Finally, the capability to perform mission maneuvers was shown with simulation results.

Several aspects could still be improved. A considerable gain in the efficiency of the system would be acquired with better coil manufacturing process, which could achieve wire packing factors closer to those reported by the wire manufacturer. This would also allow smaller margins in the design parameters. A more detailed EMI analysis would as well be beneficial, which would include a full spectrum of the magnetic field emissions instead of only focusing on the dominating frequency. However, designed and manufactured ACS satisfied all the requirements posed by the mission and it demonstrated satisfactory efficiency and performance capabilities.

## REFERENCES

- [1] M. N. Sweeting, "Modern small satellites-changing the economics of space," *Proc. IEEE*, vol. 106, no. 3, pp. 343–361, Mar. 2018.
- [2] A. Ali, M. R. Mughal, H. Ali, and L. Reyneri, "Innovative power management, attitude determination and control tile for CubeSat standard nanosatellites," *Acta Astronautica*, vol. 96, pp. 116–127, Mar./Apr. 2014.
- [3] M. R. Mughal, A. Ali, and L. M. Reyneri, "Plug-and-play design approach to smart harness for modular small satellites," *Acta Astronautica*, vol. 94, no. 2, pp. 754–764, 2014.
- [4] K. Vega, D. Auslander, and D. Pankow, "Design and modeling of an active attitude control system for CubeSat class satellites," in *Proc. AIAA Model. Simulat. Technol. Conf.*, 2009, p. 5812.
- [5] Jet Propulsion Laboratory. (2014). *Radiometer Atmospheric CubeSat Experiment (RACE)*. Accessed: Dec. 2020. [Online]. Available: <https://www.jpl.nasa.gov/cubesat/missions/race.php>
- [6] T. Neilsen, C. Weston, C. Fish, and B. Bingham, "Dice: Challenges of spinning CubeSats," in *Proc. 37th Annu. AAS Guid. Control Conf.*, 2014, pp. 387–404.
- [7] H. Ehrpais, J. Kütt, I. Sünter, E. Kulu, A. Slavinskis, and M. Noorma, "Nanosatellite spin-up using magnetic actuators: ESTCube-1 flight results," *Acta Astronautica*, vol. 128, pp. 210–216, Nov./Dec. 2016.
- [8] University of California. (2018). *The Electron Losses and Fields Investigation (ELFIN)*. Accessed: Dec. 2020. [Online]. Available: <https://elfin.igpp.ucla.edu/>
- [9] H. C. Polat, J. Virgili-Llop, and M. Romano, "Survey, statistical analysis and classification of launched CubeSat missions with emphasis on the attitude control method," *J. Small Satell.*, vol. 5, no. 3, pp. 513–530, 2016.
- [10] J. Li, M. Post, T. Wright, and R. Lee, "Design of attitude control systems for CubeSat-class nanosatellite," *J. Control Sci. Eng.*, vol. 2013, p. 4, Jan. 2013. [Online]. Available: <http://dx.doi.org/10.1155/2013/657182>
- [11] W. Storck, O. Billett, M. Jambusaria, A. Sathwani, P. Jammes, and P. J. Cutler, "A survey of micropropulsion for small satellites," in *Proc. AIAA/USU 20th Annu. Conf. Small Satell.*, 2006, p. 12.
- [12] J. C. Pascoa, O. Teixeira, and G. Filipe, "A review of propulsion systems for CubeSats," in *Advances in Aerospace Technology*, vol. 1. New York, NY, USA: ASME, Nov. 2018, Art. no. V001T03A039. [Online]. Available: <http://proceedings.asmedigitalcollection.asme.org/proceeding.aspx?doi=10.1115/IMECE2018-88174>
- [13] D. Sternberg, J. Essmiller, C. Colley, A. Klesh, and J. Krajewski, "Attitude control system for the Mars Cube One spacecraft," in *Proc. IEEE Aerosp. Conf.*, 2019, pp. 1–10.

- [14] G. Manzoni and Y. L. Brama, "CubeSat micropropulsion characterization in low earth orbit," in *Proc. 29th Annu. AIAA/USA Conf. Small Satell.*, Logan, UT, USA, 2015, pp. 1–9.
- [15] J. Praks *et al.*, "Aalto-1, multi-payload CubeSat: Design, integration and launch," *Acta Astronautica*, to be published.
- [16] A. Ali, M. R. Mughal, H. Ali, L. M. Reyneri, and M. N. Aman, "Design, implementation, and thermal modeling of embedded reconfigurable magnetorquer system for nanosatellites," *IEEE Trans. Aerosp. Electron. Syst.*, vol. 51, no. 4, pp. 2669–2679, Oct. 2015.
- [17] H. Ali, Q. Ul Islam, M. R. Mughal, R. Mahmood, M. R. Anjum, and L. M. Reyneri, "Design and analysis of a rectangular PCB printed magnetorquer for nanosatellites," *IEEE J. Miniat. Air Space Syst.*, early access, Oct. 7, 2020, doi: [10.1109/JMASS.2020.3029489](https://doi.org/10.1109/JMASS.2020.3029489).
- [18] Z. Mukhtar, A. Ali, M. R. Mughal, and L. M. Reyneri, "Design and comparison of different shapes embedded magnetorquers for CubeSat standard nanosatellites," in *Proc. Int. Conf. Comput. Electron. Electr. Eng. (ICE Cube)*, 2016, pp. 175–180.
- [19] X. Xia *et al.*, "Nanosats/CubeSats ADCS survey," in *Proc. 29th Chin. Control Decis. Conf. (CCDC)*, May 2017, pp. 5151–5158.
- [20] M. Palmroth *et al.*, "FORESAIL-1 CubeSat mission to measure radiation belt losses and demonstrate de-orbiting," *J. Geophys. Res. Space Phys.*, vol. 124, no. 7, pp. 5783–5799, Jul. 2019. [Online]. Available: <https://agupubs.onlinelibrary.wiley.com/doi/abs/10.1029/2018JA026354>
- [21] J. Gieseler *et al.*, "Radiation monitor RADMON aboard AALTO-1 CubeSat: First results," *Adv. Space Res.*, vol. 66, no. 1, pp. 52–65, 2020.
- [22] J. Praks *et al.*, "Aalto-1, multipayload CubeSat: Design, integration and launch," *Acta Astronautica*, to be published.
- [23] I. Iakubivskyi *et al.*, "Coulomb drag propulsion experiments of ESTCube-2 and FORESAIL-1," *Acta Astronautica*, vol. 177, pp. 771–783, Dec. 2020. [Online]. Available: <http://www.sciencedirect.com/science/article/pii/S0094576519314250>
- [24] H. Sakamoto *et al.*, "Verification of tether deployment system aboard CubeSat through dynamics simulations and tests," in *Proc. IEEE Aerosp. Conf.*, 2021, pp. 1–7.
- [25] J. Guo, J. Zhang, C. Yue, and F. Wang, "Modeling of the CubeSat deployment and initial separation angular velocity estimation," *Aerosp. Sci. Technol.*, vol. 95, Dec. 2019, Art. no. 105477.
- [26] P. Oleynik *et al.*, "Particle telescope aboard FORESAIL-1: Simulated performance," *Adv. Space Res.*, vol. 66, no. 1, pp. 29–41, 2020.
- [27] Hyperion Technologies B.V. *RW400 Series Reaction Wheels*. Accessed: Dec. 2020. [Online]. Available: <https://hyperiontechnologies.nl/products/rw400-series-reaction-wheel>
- [28] Blue Canyon Technologies. *Blue Canyon Technologies Is a Leading Provider of Turnkey Small Satellite*. Accessed: Dec. 2020. [Online]. Available: <https://bluecanyontech.com/components>
- [29] Hyperion Technologies B.V. *MTQ200 Series Magnetorquers*. Accessed: Dec. 2020. [Online]. Available: <https://hyperiontechnologies.nl/products/mtq200/>
- [30] Hyperion Technologies B.V. *MTQ400 Series Magnetorquers*. Accessed: Dec. 2020. [Online]. Available: <https://hyperiontechnologies.nl/products/mtq400/>
- [31] G. Space. *Single Axis Magnetorquer for Nanosatellites*. Accessed: Dec. 2020. <https://gomspace.com/shop/subsystems/attitude-orbit-control-systems/nanotorque-z-axis-internal.aspx>
- [32] J. Kraus, *Electromagnetics* (Electrical Engineering). New York, NY, USA: McGraw-Hill, 1984. [Online]. Available: <https://books.google.fi/books?id=CSJRAAAAMAAJ>
- [33] M. E. Brinson and S. Jahn, "Modelling of high-frequency inductance with Quacs non-linear radio frequency equation defined devices," *Int. J. Electron.*, vol. 96, no. 3, pp. 307–321, Mar. 2009.
- [34] T. Martin and S. Ang, "Digital control for switching converters," in *Proc. IEEE Int. Symp. Ind. Electron.*, vol. 2, 1995, pp. 480–484.
- [35] "DRV883x low-voltage H-bridge driver," Datasheet DRV8838, Texas Instrum., Dallas, TX, USA, 2012.
- [36] P. Lorrain, D. Corson, and F. Lorrain, *Electromagnetic Fields and Waves: Including Electric Circuits* (A Series of Books in Physics). Oxford, U.K.: Freeman, 1988. [Online]. Available: <https://books.google.fi/books?id=BtehQgAACAAJ>
- [37] "MSP430FR573x mixed-signal microcontrollers," Datasheet MSP430FR5738, Texas Instrum., Dallas, TX, USA, 2017.